Letter

# Laboratory evidence of the nonresonant streaming instability in the formation of quasiparallel collisionless shocks at high Alfvénic Mach number

S. Bolaños,[1] M. J.-E. Manuel,[2,*] M. Bailly-Grandvaux,[1] A. S. Bogale,[1] D. Caprioli,[3,4] S. R. Klein,[5] D. Michta,[6] P. Tzeferacos,[6] and F. N. Beg[1]

[1]*Center for Energy Research, University of California San Diego, La Jolla, California 92093, USA*
[2]*General Atomics, San Diego, California 92103, USA*
[3]*Department of Astronomy and Astrophysics, The University of Chicago, 5640 S Ellis Ave, Chicago, Illinois 60637, USA*
[4]*Enrico Fermi Institute, The University of Chicago, 5640 S Ellis Ave, Chicago, Illinois 60637, USA*
[5]*Department of Nuclear Engineering and Radiological Sciences, University of Michigan, Ann Arbor, Michigan 48109, USA*
[6]*University of Rochester, Rochester, New York 14627, USA*

(Received 24 April 2023; revised 13 October 2023; accepted 16 July 2024; published 5 September 2024)

We present an experimental investigation of the formation stage of a collisionless shock when the flow velocity is aligned with an ambient magnetic field utilizing laser-driven, super-Alfvénic plasma flows. As the flows interact, electromagnetic streaming instabilities develop. Proton deflectometry is used to visualize these electromagnetic fluctuations indicating the development of the ion-Weibel instability and the nonresonant instability. Hybrid simulations also show growth of the nonresonant instability and suggest that it provides an efficient source of dissipation for a shock.

DOI: 10.1103/PhysRevE.110.L033201

*Introduction.* Collisionless shocks are ubiquitous in our universe and are considered an ideal system to accelerate cosmic rays (CR) up to $10^{15}$eV through the diffusive shock acceleration mechanism (DSA) [1,2]. Recent observational [3,4] and numerical [5,6] studies show direct evidence that the efficiency of CR acceleration is strongly dependent on magnetic inclination and the Alfvénic Mach number ($M_A$). The magnetic inclination is the angle between the ambient magnetic field and the shock velocity. High-$M_A$ and quasiparallel orientation provide ideal conditions for efficient DSA [3,6]. Supernova remnants (SNR) with $M_A > 100$ are considered the primary source of galactic CR [7]. Interestingly, when CRs are streaming ahead of the shock with a drift velocity aligned with the ambient magnetic field, they induce the nonresonant streaming instability (NRI) [8] which amplifies the existing magnetic field and thus, alters the shock structure. In turn, the acceleration mechanism is more efficient in the CR-modified shock. This feedback mechanism illustrates the nonlinear interplay between CR and shocks. To better understand such a nonlinear system, it requires a detailed examination of collisionless dissipations. Hence, NRI has been exhaustively studied numerically in an astrophysical context [8–14]. Owing to the complexity of ion-beam streaming instabilities such as NRI and the required stringent conditions, experiments on these instabilities remain scarce. Seminal experiments in the parallel configuration [15] were performed at low Alfvénic Mach number ($M_A \sim 2-4$) and showed the role of the right-hand resonant streaming instability in shock formation. At higher $M_A$, studies suggest NRI [16] could act as the mechanism for field generation that allows the formation of the quasiparallel collisionless shocks

High-power laser facilities provide the means to study streaming instabilities and, thus, collisionless shocks in controlled laboratory experiments. When two laser-driven flows interact, the inter-ion collision time between the flows is often larger than the experimental time scale due to the high velocities ($\sim$1500 km/s) involved and allows the streaming ions to interact in a collisionless manner. In addition, laboratory investigations provide the means to experimentally diagnose the interaction *in situ* and in a controlled environment; which are lacking in observations due to the unresolvable spatial scales involved in mechanisms driving astrophysical collisionless shocks. Consequently, there has been significant interest in studying the formation of collisionless shocks in the laboratory and understanding the processes that enable the coupling between collisionless plasma flows [15,17–23]. A series of unmagnetized experiments [18,22,24] observed the growth of the ion-Weibel instability that permits the coupling between two symmetric flows, resulting in eventual shock formation and particle acceleration [22].

In this Letter, we present laboratory results of the early phase of the formation of quasiparallel shocks for $M_A > 150$, relevant to young SNR shocks. Simulations show that the surge of entropy mediating the shock formation is caused by the ion-Weibel instability and the NRI. Experimental measurements show growth of ion-Weibel filaments followed by the NRI, as inferred from proton images taken at multiple times during the evolution of the system. These observations are supported by hybrid particle-in-cell (PIC) simulations that indicate that the isotropization of the two plasmas occurs in less than ten ion gyroperiods, suggesting a substantial contribution of the NRI in the development of the shock.

*Contact author: manuelm@fusion.gat.com

 ©2024 American Physical Society

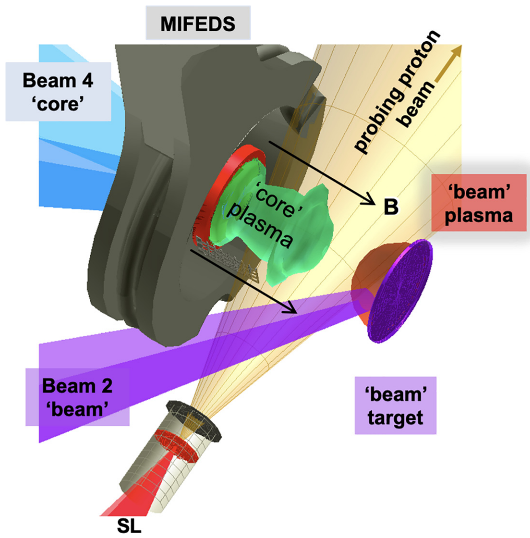


FIG. 1. Schematic of the experimental setup. The "beam" plasma (red hemisphere) interacts and propagates through the "core" plasma (green blob) in the presence of an external magnetic field (generated by MIFEDS, gray box) aligned with the flow axis of the two plasmas.

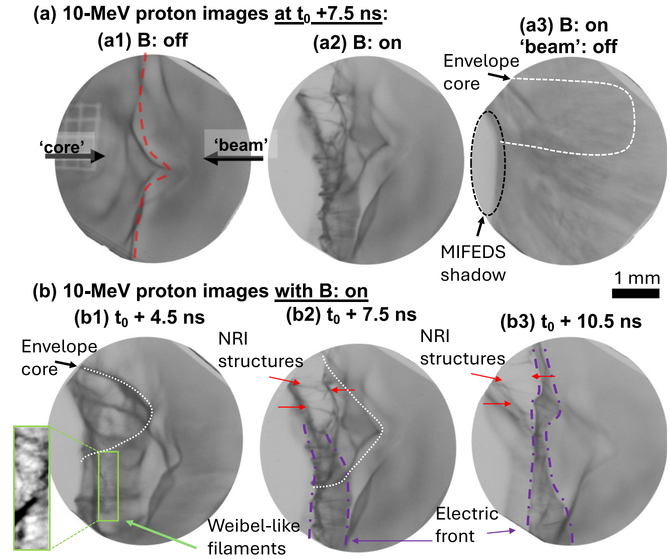


FIG. 2. 10 MeV proton images: (a) 7.5 ns after the initial asymmetric interaction ($t_0$) without external B field (a1), with the external B field (a2), and core only with the external B field (a3). Features are shifted up due to the external magnetic field. (b) 10 MeV proton images showing the temporal evolution of field structures at 4.5, 7.5, and 10.5 ns after $t_0$, (b1), (b2), and (b3), respectively. Light areas on the left-hand side in premagnetized shots are MIFEDS shadows. The white dotted lines in (a3), (b2), and (b3) are the approximate location of the core.

*Experimental setup.* Experiments were conducted at the OMEGA-EP laser facility, see Fig. 1, wherein two distinctly different plasma flows counterpropagate head on to investigate quasiparallel collisionless shock formation. First, a 4 μm thin Ti foil is driven by a 0.5 ns pulse containing 500 J. The ablation pressure launches a shock through the target and the cold ($T_i \sim T_e \sim 10-20$ eV), dense ($n_i \sim 1.5 \times 10^{19}\,\mathrm{cm}^{-3}$) plasma accelerated from the backside of the target travels toward (150 km/s) the second target. This plasma plays the role of the background, referred to as the core. The second Ti target, represented by the purple disk in Fig. 1, is driven by a 1 ns square pulse delivering 1250 J with an intensity of $\sim 5.6 \times 10^{14}\,\mathrm{W/cm}^2$. This ablation plasma, referred to as the beam, expands counterpropagatively to the core and is initiated 17 ns after the core to account for the higher velocity (1500–2000 km/s). To investigate the quasiparallel configuration, an external magnetic field parallel to flow velocity is applied using a multiloop MIFEDS [25] coil, providing a magnetic field strength of 17 T near the core target and falling off to 4 T near the beam target.

*Results.* The beam and core plasmas are modeled in a cylindrical-2D geometry using the radiative-magnetohydrodynamic code, FLASH [26,27]. Simulations of laser-driven targets using FLASH provide the ability to estimate unmeasured quantities. The plasma parameters given above and are used in the subsequent analysis, extracted from FLASH simulations, which are validated against data from the 4$\omega$-probe diagnostic suite, Nomarski interferometry and angular filter refractometry (AFR) [28], and x-ray spectrometry [29]. It shows reasonable agreement inside the core, see the Supplemental Material [30]. We note the FLASH calculations underpredict by 25% the density in the region of interaction. Simulations of the beam or core plasmas separately provide plasma conditions prior to interpenetration. As a hydrodynamic code, FLASH calculations of the two interacting flows cannot accurately model physics of the collisionless ions, but they can help to differentiate hydrodynamic and kinetic effects in experiments. Generation of the beam plasma is delayed relative to the core to account for the different flow speeds and to ensure that the interaction region of the two flows occurs near target chamber center, where diagnostics are pointed. The interpenetration of beam ions into the core plasma begins at $\sim$18.5 ns ($t_0$) following the irradiation of the core. Due to the high velocity of the beam flow, the core-ion/beam-ion mean free path is $\sim$16 cm, which is larger than the distance between the core and beam targets (6 mm); the system can thus be considered collisionless for the ions. Beam ions can stream into the core leading to the development of collisionless microinstabilities and producing self-generated electromagnetic fields that can be visualized with proton deflectometry. This technique utilizes a laminar proton backlighter [31] induced by a high-intensity laser beam (SL beam in Fig. 1) to detect electromagnetic field structures in the plasma. Protons are deflected by electromagnetic fields as they propagate through the interaction volume and the proton flux is recorded on a filtered radiochromic film (RCF) stack, providing energy resolved images. Measured proton fluence variations are attributed to electromagnetic field fluctuations in the plasma with a temporal resolution of 40 ps for 10 MeV protons.

Experimental proton images of the two-flow interaction are shown in Fig. 2. The image at $t_0 + 7.5$ ns [Fig. 2(a1)] shows that without an external magnetic field, smooth field structures form at the interface of the two flows; e.g., the triangular feature and all the vertical planar features, highlighted by the dashed red line in Fig. 2(a1). These structures are caused by the advected magnetic field likely produced by the Biermann-

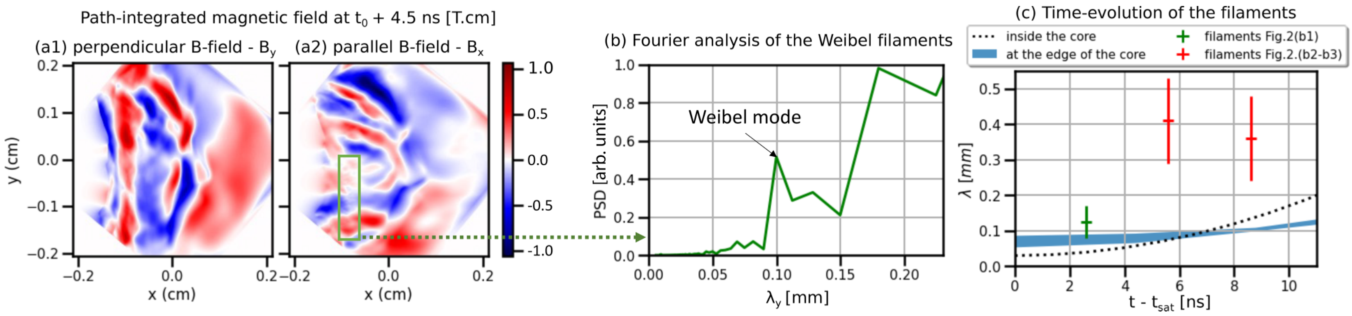


FIG. 3. (a1), (a2) reconstructed path-integrated magnetic field from the 16 MeV proton image at $t_0 + 4.5$ ns [Fig. 2(b1)]. (b) Power spectral density (PSD) analysis of Weibel-like filaments. The Fourier analysis was performed in the green rectangle of (a2). (c) Estimation of the filament size at 4.5 ns (green) and 7.5, 10.5 ns (red). The measurement is compared to the coalescence model of the ion-Weibel filaments in the plasma condition of the core center (dashed black line) and at the edge of the core (blue line). $t_{sat}$ is the saturation time and we estimate $t_{sat} = t_0 + 1.9$ ns.

battery mechanism near the beam target [32]. The magnetic field is advected efficiently with the beam plasma since it is "frozen in" ($Re_m > 1000$) to the electron fluid. The advected field piles up [see red dashed line in Fig. 2(a1)] at the core-beam interface as the beam electrons collide with the core electrons. When applying a magnetic field, the advected and piled-up field is still present within the asymmetric flow interaction, but now in the presence of filamentary field structures (scale sizes of hundreds of μm) and larger structures (1mm) in the core [Fig. 2(a2)]. When the beam plasma is not present, only faint striations are visible [Fig. 2(a3)]. The orientation and homogeneity across the image indicate that the striations result from MIFEDS fields in a vacuum. Filamentary structures are identified in the $t_0 + 4.5$ ns image by the green box in Fig. 2(b1) located at the outer edge of the core. The core position is depicted in proton images [Figs. 2(b1) and 2(b2)] by a dashed white line to show the relative position of the observed filaments. The white dotted line [Figs. 2(b1) and 2(b2)] corresponds to where the gradient of the core density is maximized according to the FLASH calculations, at $n_i \sim 0.3 \times 10^{19}$ cm$^{-3}$. The dashed line position was determined using the AFR and shadowgraphy diagnostics. Later, we observe the presence of an electrostatic front, see purple dashed lines in Figs. 2(b2) and 2(b3) as well as larger filamentary structures in the center of the core identified by red arrows in Figs. 2(b2) and 2(b3). Those filamentary structures are the result of the beam propagating through the premagnetized core since such structures are not observed in the unmagnetized interaction [Fig. 2(a1)] or when only the premagnetized core is present [Fig. 2(a3)]. A careful analysis of the filaments at the different proton energy, indicates that deflections are primary magnetic, see the Supplemental Material [30].

Path-integrated magnetic field maps are reconstructed using the PROBLEM solver [33,34] to characterize the filaments and assess their origin. The utilization of this technique is warranted because the deflections of the protons by the magnetic filaments are still smaller than the plasma scale length. Reconstructed path-integrated magnetic field components for 16 MeV protons at $t_0 + 4.5$ ns are shown in Fig. 3(a). The high-frequency filaments located on the outside of the core are denoted by the green box in Fig. 3(a2). A Fourier analysis was performed in this area to constrain the analysis to the magnetic fluctuations of interest, resulting in the power spectral density shown in Fig. 3(b). It shows the presence of a dominant mode with a wavelength of $\sim 125 \pm 45$ μm. We note that the external magnetic field induces some distortions of proton images. However, these distortions are small and encompassed in the uncertainties of the estimated wavelengths; see the Supplemental Material [30]. The inferred magnetic wavelength can be compared to analytical models or hybrid-PIC calculations to determine the instability generating B fields of this size.

Counterpropagating, unmagnetized plasma slabs have shown robust formation and growth of filamentary structures driven by the ion-Weibel instability [18,19,21,22]. Previous works demonstrated that the initial plasma parameters set the growth of the filamentation [35,36], and then a coalescence of the current filaments occurs once the instability reaches saturation. In order to estimate the dominant mode and the growth time, we compute the dispersion relation using a kinetic formalism derived by Ruyer *et al.* [36] and plasma parameters derived from benchmarked FLASH calculations. The filaments are located 0.8mm–1.2mm away radially from the center of the "core" plasma. At this location, the ion density of the core varies from $0.7 \times 10^{18}$cm$^{-3}$ to $0.3 \times 10^{19}$cm$^{-3}$. Considering the density of the core in the middle of the green box ($\sim 10^{18}$cm$^{-3}$, $Z^* \sim 7$) and the density of the beam ($\sim 10^{17}$cm$^{-3}$, $Z^* \sim 20$) at the time of the initial interaction ($t_0$), we estimate the dominant wavelength of ion-Weibel filaments to be $\sim 80$ μm at the end of the linear phase ($t_0 + 1.9$ ns). Here, the dominant mode is the mode maximizing the saturated magnetic field described by the trapping criteria [37] given by $B_{sat} = m_i \Gamma^2(k)/(Z^* e k v)$, where $\Gamma$ is the Weibel growth rate, $v$ is the relative bulk velocity, $e$ is the elementary charge, and $k$ is the filament wavenumber. Filament wavelength scales as $\sim \delta_i = \sqrt{c^2 m_i / 4\pi n_i Z^{*2} e^2}$, where $\delta_i$ is the ion inertial length. Figure 3(c) shows the temporal evolution of the filament wavelength using the coalescence model [36] (blue band). The estimated wavelength has been plotted with a band to indicate the uncertainty due to the core density variation (from $0.7 \times 10^{18}$cm$^{-3}$ to $0.3 \times 10^{19}$cm$^{-3}$) at the location of the filaments depicted by the green box in Fig. 2(b1). Note that in the center of the core, the density reaches $n_i \sim 1.5 \times 10^{19}$cm$^{-3}$, implying a dominant wavelength of $\sim 30$ μm at saturation of the ion-Weibel instability, and they are predicted to merge into 52 μm wavelength filaments over the course of 4 ns. Such a size (tens of μm) is out of the resolution of the diagnostic. From this analysis, it is clear that filamentary field structures observed at the edge of the core at $t_0 + 4.5$ ns are consistent with the collisionless ion-Weibel instability.

At later times, large filamentlike patterns inside the core plasma are observed in proton images, as indicated by red arrows in Figs. 2(b2) and 2(b3). We applied the same Fourier analysis, restricted to the area of these filaments and away from the electrostatic front [38] [see purple dashed lines in Figs. 2(b2) and 2(b3)] to avoid interference of the electrostatic field with the magnetic fluctuation analysis. The dominant wavelengths inferred are $\sim 410 \pm 120\,\mu$m at $t_0 + 7.5$ ns, and $\sim 360 \pm 120\,\mu$m at $t_0 + 10.5$ ns; see the Supplemental Material [30]. The large uncertainty of the filamentary wavelength is due to the limited region of the analysis. Filaments of this size do not match the coalescence model for ion-Weibel filaments inside the core, see the black dotted line in Fig. 3(c), where the expected sizes at these times are $\sim 70\,\mu$m and $\sim 130\,\mu$m at $t_{sat} + 5.6$ ns and $t_{sat} + 8.6$ ns, respectively. This discrepancy cannot be explained by the 25% underprediction in the density from the FLASH calculations. Note that the blue band and black dotted line correspond to a density ranging from $0.7 \times 10^{18}\text{cm}^{-3}$ to $1.5 \times 10^{19}\text{cm}^{-3}$. Although the early filaments at the edge of the core are the results of the ion-Weibel instability, a different kinetic instability is at the origin of the late-time filamentary structure observed inside the core.

In the premagnetized case, we expect a strong beam streaming in the core plasma parallel to the existing magnetic field. Such a configuration and the length scale of the magnetic filaments (few ion inertial length) suggest the establishment of the ion-beam instability, especially NRI with a growth rate close to $\gamma \sim \Omega_0 \sim 0.14$ rad/ns due to the high velocity of the flow [39] where $\Omega_0$ is the core ion gyrofrequency. We calculated the dispersion relation for an ion beam propagating in a background plasma with drift velocity parallel to an external magnetic field, as formulated by Gary *et al.* [40] [Eq. (8.1.7)]. These calculations use the FLASH-predicted plasma parameters at $t_0$, see the black dotted line in Fig. 4(a). The dominant mode found at $\sim -0.2\delta_i$ indicates the growth of the NRI instability.

Hybrid-PIC simulations were conducted using the AKA [41] code in 3D to characterize magnetic field generation under experimentally relevant plasma conditions. AKA treats the electrons as an inertialess fluid and the ions as macroparticles following the PIC scheme. Figures 4(b1) and 4(b2) show two components of magnetic fields calculated with AKA using estimated plasma parameters in the central core at $t_0$. It confirms the growth of magnetic waves induced by kinetic instabilities. Temporal tracking of the waves indicates that they travel in the counterpropagative direction of the beam. The waves are right-hand polarized ($\omega > 0$) and present negative helicity ($k < 0$), see helicity decomposition in Fig. 4(a), consistent with NRI which produces right-hand polarized waves counterpropagating to the beam [13,16]. A comparison of the analytically calculated dominant mode is in good agreement with the helicity decomposition, illustrating that B fields observed in hybrid-PIC calculations are dominated by the NRI. Green lines in Fig. 4(c) present the dominant mode ($\lambda_y$) of $B_x$. The dashed green line is the dominant mode inferred from simulated proton radiographs of the 3D field structure using the same imaging geometry as

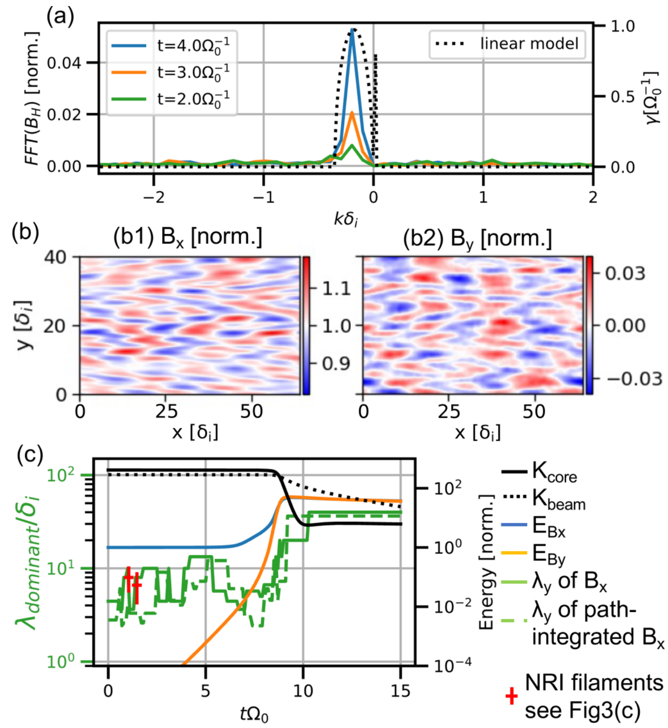


FIG. 4. (a) Calculated growth using the equation dispersion from Gary *et al.* [40] and the plasma parameters at $t_0$ (black dotted line). Solid lines are helicity-decomposed spectra of the perpendicular magnetic field at different times from simulation. (b1), (b2) Parallel and perpendicular components of the magnetic field calculated by the hybrid PIC code for plasma conditions taken at $4\Omega_0^{-1}$. (c) Temporal evolution of plasma parameters: core kinetic energy (solid black line) and beam kinetic energy (dotted black line), parallel magnetic energy (blue line), perpendicular magnetic energy (orange line), and green lines are the wavelength ($\lambda_y$) of the dominant mode for $B_x$ (solid) and $B_x$ along the proton path as in the experiment (dashed). The red crosses are the NRI wavelength measured experimentally.

the experiment. Experimental measurements of filament sizes [red crosses in Fig. 4(c)], taken at times $< 2\Omega_0^{-1}$ (i.e., growth is expected to be in the linear regime), are consistent with hybrid-PIC calculations.

Therefore, the large filamentary structures indicated by red arrows in proton images shown in Figs. 2(b2) and 2(b3) are experimental evidence of the NRI in a parallel configuration.

While further evolution of the NRI was not explored in experiments, hybrid-PIC simulations can provide insight into the expected behavior at later times. A strong slowdown of the beam and core ions occurs at later times, mediated by the NRI. The free energy in the beam and core dissipates and heats the plasma efficiently at saturation, $8.5\Omega_0^{-1}$. Later ($t > 10\Omega_0^{-1}$), the magnetic field turns isotropic, indicating the formation of turbulence. A fast slowdown of the beam and core plasma, along with the presence of turbulent B fields, suggests that NRI would efficiently drive the formation of the quasiparallel shock in this configuration.

Both the ion-Weibel and nonresonant instabilities play a role in magnetized collisionless shock formation in a parallel configuration. Due to faster growth rates, B-field generation at early times is dominated by the ion-Weibel instability. This instability quickly saturates at $B \sim 4$ T for these experimental conditions, and then the nonlinear regime begins wherein the filament size increases. Previous works [35,42] demonstrated that an increase of the magnetic strength by a factor of 3–10 occurs after saturation in symmetric inhomogeneous plasmas. In this experiment, amplification after saturation is expected to be less due to the uniform background plasma and asymmetric geometry. Filamentary B fields driven by the NRI are observed at later times due to the slower growth rate. NRI growth is still in the linear regime at the times probed in this work. The NRI saturates when the magnetic field reaches a few times the external magnetic field, $\sim$50 T, here. We thus expect the NRI to be the dominant dissipation mechanism after few ion gyroperiods.

*Summary.* An experimental platform to study quasiparallel, high-$M_A$ shocks was developed utilizing asymmetric plasma flows generated by laser-driven targets. Magnetic fields generated by kinetic ion-streaming instabilities were visualized using proton images taken at multiple times during the interaction. In the presented work, the initial phases of shock formation were studied, but the shock could not be fully formed in the time scale of the experiment. Through a detailed Fourier analysis of proton images, and comparisons with analytic theory and hybrid-PIC simulations, the NRI and ion-Weibel instability were identified as the most likely source of the observed filamentary field structures and capable of mediating shock formation. This work demonstrates the existence and characterization of B fields generated by the NRI for highly superalfvénic flows in the context of quasiparallel shock formation and provides a path for future experiments and to create fully formed shocks to observe and study particle acceleration in these systems.

*Acknowledgments.* The authors express their gratitude to the engineering staff and senior management at LLE for their support in the successful execution of the experiments discussed herein. This work was supported by the DOE Office of Science, Fusion Energy Sciences under Contract No. DE-SC0021061: the LaserNetUS initiative at the Omega Laser Facility. This project is supported by the Department of Energy, National Nuclear Security Administration (NNSA) under Awards No. DE-NA0003842 and No. DE-NA0004147 as part of the Center for Matter under Extreme Conditions (CMEC), an NNSA Center of Excellence. This work of D.C. was supported by the NSF through the Grant No. PHY-2010240.

[1] A. R. Bell, The acceleration of cosmic rays in shock fronts - I, Mon. Not. R. Astron. Soc. **182**, 147 (1978).
[2] R. D. Blandford and J. P. Ostriker, Particle acceleration by astrophysical shocks, The Astrophys. J. **221**, L29 (1978).
[3] A. Johlander *et al.*, Ion acceleration efficiency at the earth's bow shock: Observations and simulation results, The Astrophys. J. **914**, 82 (2021).
[4] R. Giuffrida, M. Miceli, D. Caprioli, A. Decourchelle, J. Vink, S. Orlando, F. Bocchino, E. Greco, and G. Peres, The supernova remnant SN 1006 as a Galactic particle accelerator, Nat. Commun. **13**, 5098 (2022).
[5] J. Giacalone, D. Burgess, S. J. Schwartz, and D. C. Ellison, Ion injection and acceleration at parallel shocks - comparisons of self-consistent plasma simulations with existing theories, The Astrophys. J. **402**, 550 (1993).
[6] D. Caprioli and A. Spitkovsky, Simulations of ion acceleration at non-relativistic shocks. I. Acceleration efficiency, Astrophys. J. **783**, 91 (2014).
[7] M. Ackermann *et al.*, Detection of the characteristic pion-decay signature in supernova remnants, Science **339**, 807 (2013).
[8] A. R. Bell, Turbulent amplification of magnetic field and diffusive shock acceleration of cosmic rays, Mon. Not. R. Astron. Soc. **353**, 550 (2004).
[9] M. A. Riquelme and A. Spitkovsky, Nonlinear study of Bell's cosmic ray current-driven instability, Astrophys. J. **694**, 626 (2009).
[10] Y. Ohira, B. Reville, J. G. Kirk, and F. Takahara, Two-dimensional particle-in-cell simulations of the nonresonant, cosmic-ray-driven instability in supernova remnant shocks, Astrophys. J. **698**, 445 (2009).
[11] L. Gargaté, R. A. Fonseca, J. Niemiec, M. Pohl, R. Bingham, and L. O. Silva, The nonlinear saturation of the non-resonant kinetically driven streaming instability, Astrophys. J. **711**, L127 (2010).
[12] E. G. Zweibel and J. E. Everett, Environments for magnetic field amplification by cosmic rays, Astrophys. J. **709**, 1412 (2010).
[13] A. Marret, A. Ciardi, R. Smets, and J. Fuchs, On the growth of the thermally modified non-resonant streaming instability, Mon. Not. R. Astron. Soc. **500**, 2302 (2020).
[14] G. Zacharegkas, D. Caprioli, C. Haggerty, S. Gupta, and B. Schroer, Modeling the saturation of the Bell instability using hybrid simulations, The Astrophys. J. **967**, 71 (2024).
[15] P. V. Heuer, M. S. Weidl, R. S. Dorst, D. B. Schaeffer, S. K. Tripathi, S. Vincena, C. G. Constantin, C. Niemann, and D. Winske, Laser-produced plasmas as drivers of laboratory collisionless quasi-parallel shocks, Phys. Plasmas **27**, 042103 (2020).
[16] M. S. Weidl, D. Winske, and C. Niemann, Three regimes and four modes for the resonant saturation of parallel ion-beam instabilities, The Astrophys. J. **873**, 57 (2019).
[17] Y. Kuramitsu *et al.*, Time evolution of collisionless shock in counterstreaming laser-produced plasmas, Phys. Rev. Lett. **106**, 175002 (2011).
[18] C. M. Huntington *et al.*, Magnetic field production via the Weibel instability in interpenetrating plasma flows, Phys. Plasmas **24**, 041410 (2017).
[19] G. F. Swadling *et al.*, Measurement of kinetic-scale current filamentation dynamics and associated magnetic fields in interpenetrating plasmas, Phys. Rev. Lett. **124**, 215001 (2020).
[20] D. B. Schaeffer, W. Fox, R. K. Follett, G. Fiksel, C. K. Li, J. Matteucci, A. Bhattacharjee, and K. Germaschewski, Direct observations of particle dynamics in magnetized collisionless shock precursors in laser-produced plasmas, Phys. Rev. Lett. **122**, 245001 (2019).
[21] J. S. Ross *et al.*, Characterizing counter-streaming interpenetrating plasmas relevant to astrophysical collisionless shocks, Phys. Plasmas **19**, 056501 (2012).

[22] F. Fiuza *et al.*, Electron acceleration in laboratory-produced turbulent collisionless shocks, Nat. Phys. **16**, 916 (2020).

[23] W. Yao *et al.*, Laboratory evidence for proton energization by collisionless shock surfing, Nat. Phys. **17**, 1177 (2021).

[24] W. Fox, G. Fiksel, A. Bhattacharjee, P. Y. Chang, K. Germaschewski, S. X. Hu, and P. M. Nilson, Filamentation instability of counterstreaming laser-driven plasmas, Phys. Rev. Lett. **111**, 225002 (2013).

[25] O. V. Gotchev, J. P. Knauer, P. Y. Chang, N. W. Jang, M. J. Shoup, D. D. Meyerhofer, and R. Betti, Seeding magnetic fields for laser-driven flux compression in high-energy-density plasmas, Rev. Sci. Instrum. **80**, 043504 (2009).

[26] B. Fryxell, K. Olson, P. Ricker, F. X. Timmes, M. Zingale, D. Q. Lamb, P. MacNeice, R. Rosner, J. W. Truran, and H. Tufo, FLASH: An adaptive mesh hydrodynamics code for modeling astrophysical thermonuclear flashes, Astrophys. J. Suppl. Ser. **131**, 273 (2000).

[27] P. Tzeferacos, M. Fatenejad, N. Flocke, C. Graziani, G. Gregori, D. Lamb, D. Lee, J. Meinecke, A. Scopatz, and K. Weide, FLASH MHD simulations of experiments that study shock-generated magnetic fields, High Energy Density Phys. **17**, 24 (2015).

[28] D. Haberberger, S. Ivancic, S. X. Hu, R. Boni, M. Barczys, R. S. Craxton, and D. H. Froula, Measurements of electron density profiles using an angular filter refractometer, Phys. Plasmas **21**, 056304 (2014).

[29] M. Millecchia, S. P. Regan, R. E. Bahr, M. Romanofsky, and C. Sorce, Streaked x-ray spectrometer having a discrete selection of Bragg geometries for omega, Rev. Sci. Instrum. **83**, 10E107 (2012).

[30] See Supplemental Material at http://link.aps.org/supplemental/10.1103/PhysRevE.110.L033201 for the in-depth presentation of the data analysis and simulation setup, which includes Refs. [14–16,26–29,33–35,43–48].

[31] P. Bolton *et al.*, Instrumentation for diagnostics and control of laser-accelerated proton (ion) beams, Physica Medica **30**, 255 (2014).

[32] D. D. Ryutov, N. L. Kugland, M. C. Levy, C. Plechaty, J. S. Ross, and H. S. Park, Magnetic field advection in two interpenetrating plasma streams, Phys. Plasmas **20**, 032703 (2013).

[33] A. F. A. Bott, C. Graziani, P. Tzeferacos, T. G. White, D. Q. Lamb, G. Gregori, and A. A. Schekochihin, Proton imaging of stochastic magnetic fields, J. Plasma Phys. **83**, 905830614 (2017).

[34] Problem solver: https://github.com/flash-center/problem

[35] M. J.-E. Manuel *et al.*, Experimental evidence of early-time saturation of the ion-Weibel instability in counterstreaming plasmas of CH, Al, and Cu, Phys. Rev. E **106**, 055205 (2022).

[36] C. Ruyer, L. Gremillet, A. Debayle, and G. Bonnaud, Nonlinear dynamics of the ion Weibel-filamentation instability: An analytical model for the evolution of the plasma and spectral properties, Phys. Plasmas **22**, 032102 (2015).

[37] R. C. Davidson, D. A. Hammer, I. Haber, and C. E. Wagner, Nonlinear development of electromagnetic instabilities in anisotropic plasmas, Phys. Fluids **15**, 317 (1972).

[38] The nature of this structure was inferred from a thorough analysis of proton images at multiple energies, detailed in the Supplemental Material [30].

[39] K. B. Quest, Theory and simulation of collisionless parallel shocks, J. Geophys. Res. **93**, 9649 (1988).

[40] S. P. Gary, *Theory of Space Plasma Microinstabilities* (Cambridge University Press, 1993), p. 181.

[41] A. Sladkov, R. Smets, N. Aunai, and A. Korzhimanov, Numerical study of non-gyrotropic electron pressure effects in collisionless magnetic reconnection, Phys. Plasmas **28**, 072108 (2021).

[42] A. Grassi and F. Fiuza, Efficient generation of turbulent collisionless shocks in laser-ablated counter-streaming plasmas, Phys. Rev. Res. **3**, 023124 (2021).

[43] C. Niemann, W. Gekelman, C. G. Constantin, E. T. Everson, D. B. Schaeffer, A. S. Bondarenko, S. E. Clark, D. Winske, S. Vincena, B. V. Compernolle, and P. Pribyl, Observation of collisionless shocks in a large current-free laboratory plasma, Geophys. Res. Lett. **41**, 7413 (2014).

[44] P. Angland, D. Haberberger, S. T. Ivancic, and D. H. Froula, Angular filter refractometry analysis using simulated annealing, Rev. Sci. Instrum. **88**, 103510 (2017).

[45] M. J. Manuel, C. C. Kuranz, A. M. Rasmus, S. R. Klein, M. J. MacDonald, M. R. Trantham, J. R. Fein, P. X. Belancourt, R. P. Young, P. A. Keiter, R. P. Drake, B. B. Pollock, J. Park, A. U. Hazi, G. J. Williams, and H. Chen, Experimental results from magnetized-jet experiments executed at the Jupiter laser facility, High Energy Density Phys. **17**, 52 (2015).

[46] Neutrino software: https://github.com/neutrinotoolkit/neutrino.

[47] D. B. Schaeffer, W. Fox, D. Haberberger, G. Fiksel, A. Bhattacharjee, D. H. Barnak, S. X. Hu, K. Germaschewski, and R. K. Follett, High-mach number, laser-driven magnetized collisionless shocks, Phys. Plasmas **24**, 122702 (2017).

[48] J. J. MacFarlane, I. E. Golovkin, P. Wang, P. R. Woodruff, and N. A. Pereyra, SPECT3D - A multi-dimensional collisional-radiative code for generating diagnostic signatures based on hydrodynamics and PIC simulation output, High Energy Density Phys. **3**, 181 (2007).